

In situ synthesis of AgI/SnS₂ heterojunction photocatalysts with superior photocatalytic activity

Qiang Li^{1,2,*}, Kang Wang^{1,2}, Xiaoxiao Lu^{1,2}, Rui Luo^{1,2}, Min Zhang^{1,2},
Chaopeng Cui^{1,2} and Guangping Zhu^{1,2}

¹ College of Physics and Electronic Information, Huaibei Normal University, Huaibei, 235000, P.R. China

² Anhui Province Key Laboratory of Pollutant Sensitive Materials and Environmental Remediation, Huaibei Normal University, Huaibei, 235000, P.R. China

*E-mail: qiangli@chnu.edu.cn

Received: 24 April 2020 / Accepted: 22 June 2020 / Published: 10 August 2020

In present study, novel visible-light-driven photocatalyst AgI/SnS₂ heterojunctions were prepared with hydrothermal-precipitation method. The resulting AgI/SnS₂ heterojunctions exhibited superior and stable visible photocatalytic activity on Rhodamine B (RhB) removal. The optimal heterojunction with 4:1 mass ratio of AgI: SnS₂ exhibited the highest rate constant of 0.064 min⁻¹ for removal of RhB, which was about 2.1 and 3.4 times as much as pure AgI and SnS₂, respectively. In addition, the study by photoluminescence spectroscopy (PL) indicated that the improvement of the photocatalytic efficiency could be mainly owing to the truth that the photogenerated carriers were separated and transferred effectively, resulted from the appropriate band gap match of AgI and SnS₂. In addition, it was found that •O₂⁻ radicals and h⁺ were the main oxidative species responsible for removal of RhB. These features demonstrate that AgI/SnS₂ heterojunction has great application potentials for pollutants removal from wastewater.

Keyword: SnS₂ nanosheets; AgI nanoparticles; Heterojunctions; Photocatalysis

1. INTRODUCTION

In the last few decades, semiconductor photocatalysis aroused great interest for the purpose of alleviating the problems of global environmental pollution and energy crisis [1-4]. Hence, exploiting high-performance photocatalysts has become a hotspot in the research fields. So far, lots of researchers have developed various semiconductor materials as photocatalysts in several different ways [5-9]. Nevertheless, traditional semiconductor materials, such as TiO₂, ZnO, and NaTaO₃, only can respond to the ultraviolet light, which greatly hinder their potential in large-scale applications[10-12]. For the

purpose of making full use of natural solar energy, it is an urgent need to develop new-type and efficient visible-light-response (VLR) photocatalysts.

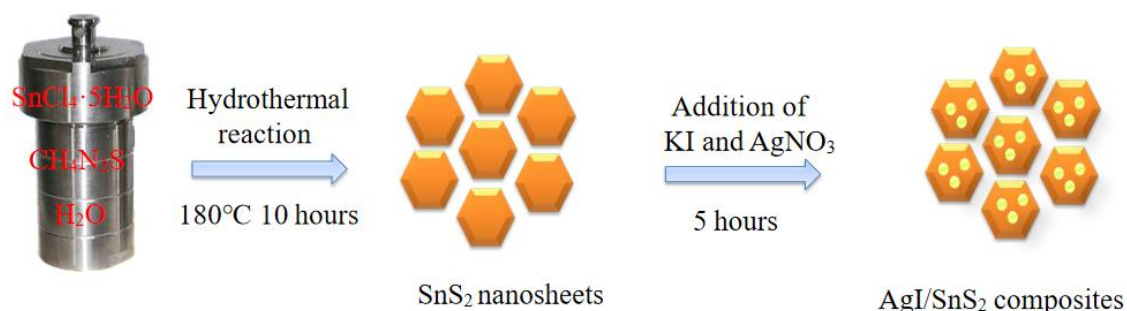
Recently, as VLR photocatalysts, metal sulfide semiconductors have attracted widespread interest [13-16]. Among them, SnS₂ has emerged as a promising candidate for photocatalytic applications because of its unique physicochemical properties, including good chemical stability, small band gap (1.91~2.35 eV) for wide photon absorption as well as suitable band-edge positions for redox reactions ($E_{CB} = -0.94$ eV, $E_{VB} = 1.26$ eV) [17, 18]. Accordingly, a variety of SnS₂ microstructures with various morphologies have been successfully synthesized, such as nanoparticles [16], nanosheets [19, 20], nanoflowers [21] and so on. Notwithstanding numerous efforts had been made in the synthesis of SnS₂, the photoactivity of single SnS₂ was still far from satisfactory because of the fast recombination of charge. In order to overcome the inherent defect of SnS₂ and further improved its photocatalytic performances, many strategies such as doping metals [22, 23], building semiconductor heterostructures [24-26], have been developed to enhance the photocatalytic performances of the single SnS₂. Among them, construction of SnS₂-based heterojunctions was verified as an effective and constructive strategy in promoting the separation efficiency of photoinduced carriers, consequently enhancing photocatalytic activity. For example, Qiu et al. synthesized BiOBr supported on SnS₂, which exhibited largely enhanced photocatalytic efficiency with irradiation of visible light compared to individual catalyst [17].

AgI was a kind of significant photosensitive material, which was usually employed in the field of photography. It displayed outstanding photocatalytic property in the removal of tetracycline, disinfection and the reduction of Cr (VI) [27-29]. Regrettably, the photocatalytic activity of pure AgI photocatalyst was still hindered by its low stability and poor dispersivity [1, 27]. Thus, more efforts are needed to surmount the abovementioned limitations to make it applicable in actual use. Fortunately, it has been demonstrated that loading of AgI nanoparticles (NPs) on the surface of other semiconductors to form heterojunctions can strengthen both stability and photoactivity of AgI. Therefore, multifarious AgI-based hybrid photocatalysts materials were fabricated and applied in environmental purification, such as AgI/g-C₃N₄[30], AgI/Bi₂O₃ [31], AgI/CeO₂ [32] and so on. Hence, combining AgI with SnS₂ would be a feasible way to improve the photocatalytic performances of AgI. Moreover, the energy band structures of AgI match well with those of SnS₂, which has a synergistic effect on the separation and transfer of photoexcited carriers. Thus, AgI/SnS₂ heterostructure composites could make up the shortcomings of the single AgI and SnS₂, which would exhibit outstanding photoactivity for organic pollutant removal. However, as far as we know, there are few reports on the synthesis and investigation of AgI/SnS₂ hybrid materials.

In present study, AgI NPs modified SnS₂ nanosheets (AgI/SnS₂) hybrid photocatalysts were fabricated for the first time through applying the hydrothermal and deposition-precipitation route, and the effect of loading amount of AgI on the photocatalytic performance of SnS₂ was investigated in detail. The resulting AgI/SnS₂ composites presented considerable improvement on the photoactivity for the removal of RhB with illumination of visible light in contrast to the pure AgI and SnS₂. The enhancement of photocatalytic performances could originate from the higher separation and migration efficiency of photoexcited carriers derived from the type II band alignment. Ultimately, a possible photocatalytic mechanism was proposed and discussed.

2. EXPERIMENT

2.1 Preparation of catalysts.



Scheme 1. Schematic illustration of the formation of AgI/SnS₂ composites.

The AgI/SnS₂ composites were fabricated through a hydrothermal-precipitation method as illustrated in Scheme 1. SnS₂ nanoflakes were in advances synthesized through a hydrothermal process according to a previous literature[33]. Typically, SnCl₄·5H₂O (6 mmol) and CH₄N₂S (39.4 mmol) were added in 70 mL distilled water under vigorous magnetic stirring for 0.5 hour. Then the mixture was transferred into a 100 mL autoclave, followed by solvothermal treatment at 180°C for 10 hours. When the reactor was cooled to room temperature, the resultant was collected by centrifugation, and rinsed for 5 times with distilled water and absolute ethanol, respectively. Finally, the obtained materials were dried overnight at 60 °C. AgI nanoparticles were decorated onto the surface of SnS₂ nanoflakes through a simple deposition and precipitation process. In a typical procedure, 1 mmol SnS₂ powder as well as a certain amount of KI was dispersed into 60 mL deionized water by ultrasonic for 30 min. Then 20 ml AgNO₃ (0.1 M) was dripped into above solution with magnetically stirring in dark. After stirring for 5 hours, the precipitate was collected and washed several times with ethanol and deionized water, then the precipitate was dried in a vacuum oven at 60°C for overnight. The preparation of AgI/SnS₂ with different mass percentage of AgI (30, 50, 80 and 90 wt%) were labeled as (30 wt%) AgI/SnS₂, (50 wt%) AgI/SnS₂, (80 wt%) AgI/SnS₂ and (90 wt%) AgI/SnS₂. Similarly, neat AgI were synthesized by a similar method without addition of SnS₂.

2.2 Characterizations.

The phase structure of the as-prepared samples was characterized by X-ray diffractometer (XRD) with irradiation of Cu K α X-ray ($\lambda=1.5418\text{\AA}$). The microstructure and elemental composition of AgI/SnS₂ heterojunctions were elucidated using Field Emission scanning electron microscopy (FESEM, SU8220) equipped with an energy-dispersive X-ray spectrometer (EDS). Transmission electron microscopy (TEM) images were conducted on a JEOL-2010 microscopy equipped with an acceleration voltage of 200 kV. X-ray photoelectron spectroscopy (XPS) measurements were performed on a Thermo Scientific ESCALab250Xi using 200 W monochromated Al K α radiation. The optical absorption characteristics were determined with UV-Vis diffuse reflection spectra by using a

PerkinElmer Lambda 950 spectrophotometer. Photoluminescence (PL) spectra were tested via a fluorescence spectrophotometer by Edinburgh FS920 spectrophotometer.

2.3 Photocatalytic activity

The photocatalytic efficiency for the removal of organic dyes over AgI/SnS₂ heterojunctions was studied under visible light irradiation supplied by a 500 W xenon lamp, which equipped with a cutoff filter (400 nm) to filter the UV lights. Typically, 50 mg of catalysts were dispersed in rhodamine B (RhB) solution (100 ml, 15 mg/L) in a 250 mL reactor. The adsorption-desorption equilibrium was reached via vigorous stirring in darkness for one and half hours. Then the solutions were irradiated with visible light. At given time intervals, five milliliters of the solutions were sampled and centrifugated (10000 rpm). Then the supernatants were analyzed using a UV-vis spectrophotometer to detect the concentration variations of RhB solution at the absorption wavelength of 554 nm. For investigation the active species involved in the reaction system, the quenching experiments were executed by adding various quenchers.

3. RESULTS AND DISCUSSION

Fig. 1 shows the XRD patterns of as-prepared SnS₂, AgI and AgI/SnS₂ composites with different contents of AgI. Clearly, five distinct diffraction peaks belong to pure SnS₂ could be readily indexed to hexagonal phase of SnS₂ (JCPDS card no. 22-0951)[34]. The sharp and strong peaks indicated the high crystallinity.

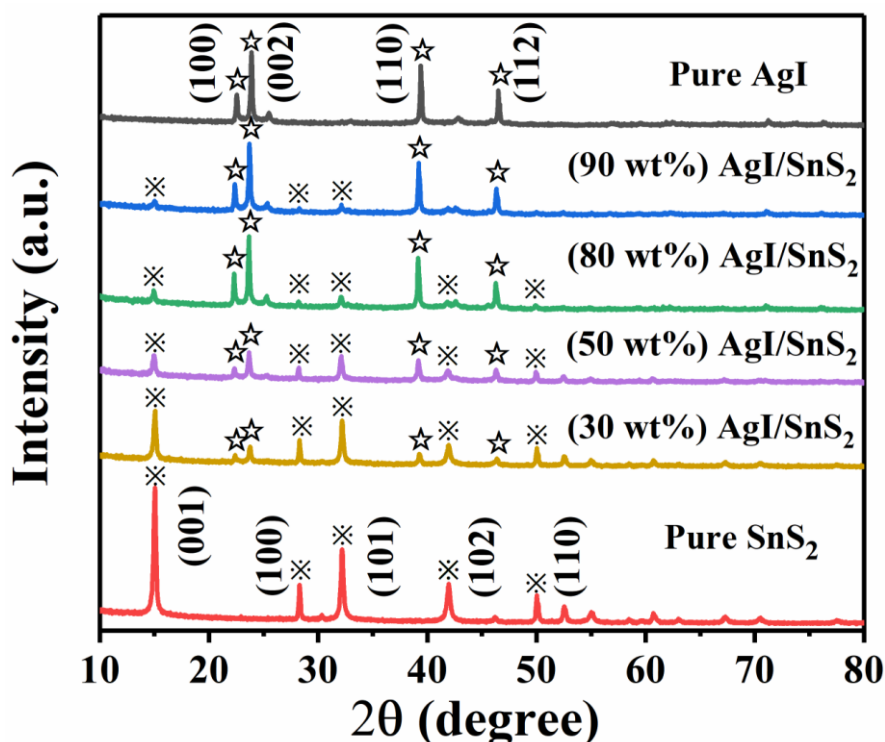


Figure 1. XRD pattern of AgI, SnS₂ and AgI/SnS₂ composites.

As for pure AgI, the main diffraction peaks located at 22.3° , 23.7° , 25.4° , 39.2° , 42.6° and 46.3° were belonged to the (100), (002), (101), (110), (103) and (112) planes of hexagonal crystal phase of AgI (JCPDS card no.09-0374)[35], respectively. The XRD patterns of AgI/SnS₂ composites revealed that the diffraction peaks of AgI and SnS₂ both can be clearly observed. No other impurity characteristic peaks were detected. Furthermore, the intensities of the diffraction peak ascribed to AgI increased with the mass percentage of AgI increase from 30 to 90% in the composites, whereas those of SnS₂ decreased simultaneously. These facts revealed the as-prepared composites were only composed of AgI and SnS₂.

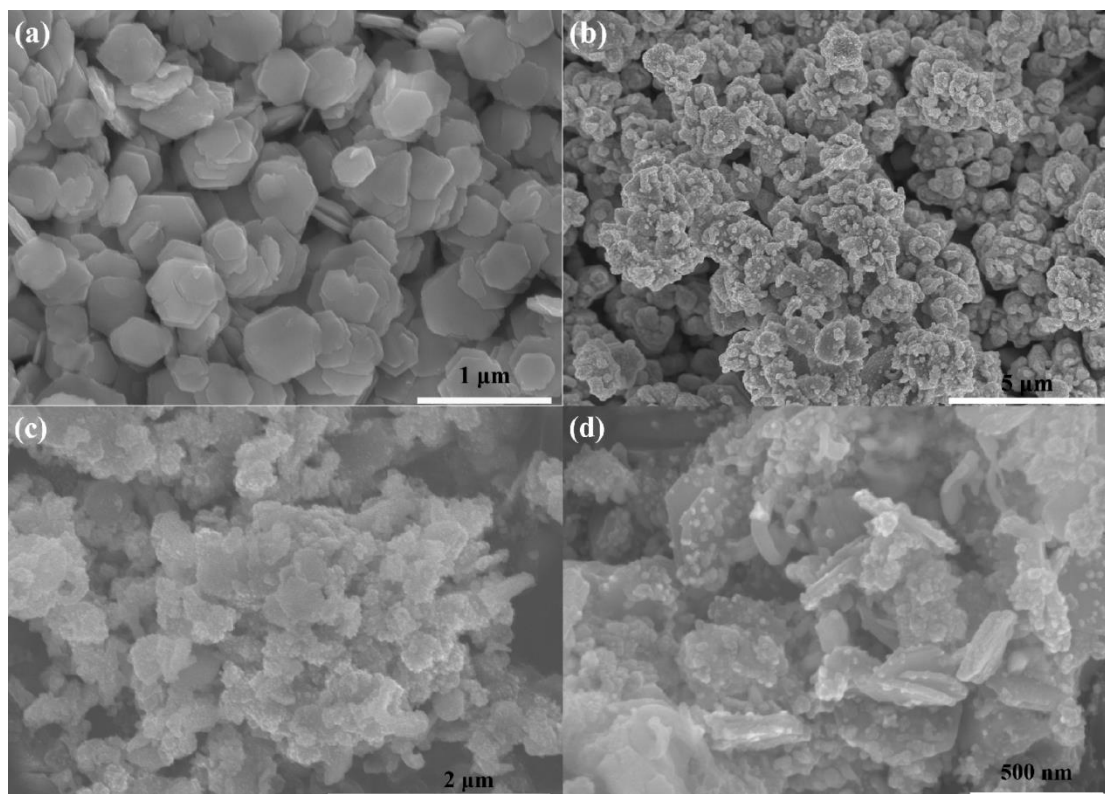


Figure 2. Typical SEM images of SnS₂ (a), AgI (b) and AgI/SnS₂ composites (c-d).

The morphologies and microstructures of all as-obtained catalysts were characterized by using FESEM. Fig. 2 presents SEM images of AgI, SnS₂ as well as AgI/SnS₂ composite. Obviously, the pristine SnS₂ (Fig. 2a) revealed a uniform sheet-like morphology with a smooth surface, and the sizes were in the range of 300 to 800 nm. Meanwhile, the as-synthesized AgI (Fig. 2b) were composed of large and irregular particles. The SEM images of AgI/SnS₂ composites were presented in Fig. 2c and d. It was clearly that after precipitation of AgI NPs on SnS₂ nanosheets, the surface of SnS₂ nanosheets became rough (Fig. 2c). The enlarged SEM image of AgI/SnS₂ in Fig. 2d clearly shows that AgI NPs were highly dispersed on the surface of SnS₂ nanosheets.

The composition and microstructure of AgI/SnS₂ were further studied by electron dispersive spectroscopy (EDS) mapping (Fig. 3). The EDS elemental mapping presented a homogeneous distribution of Ag, I, Sn and S elements in AgI/SnS₂ hybrid materials. Moreover, it could also be observed that Ag and I elements resulting from AgI evenly dispersed on the surface of SnS₂

nanosheets. These results suggested AgI and SnS₂ combined well, which was contribute to form a heterostructure.

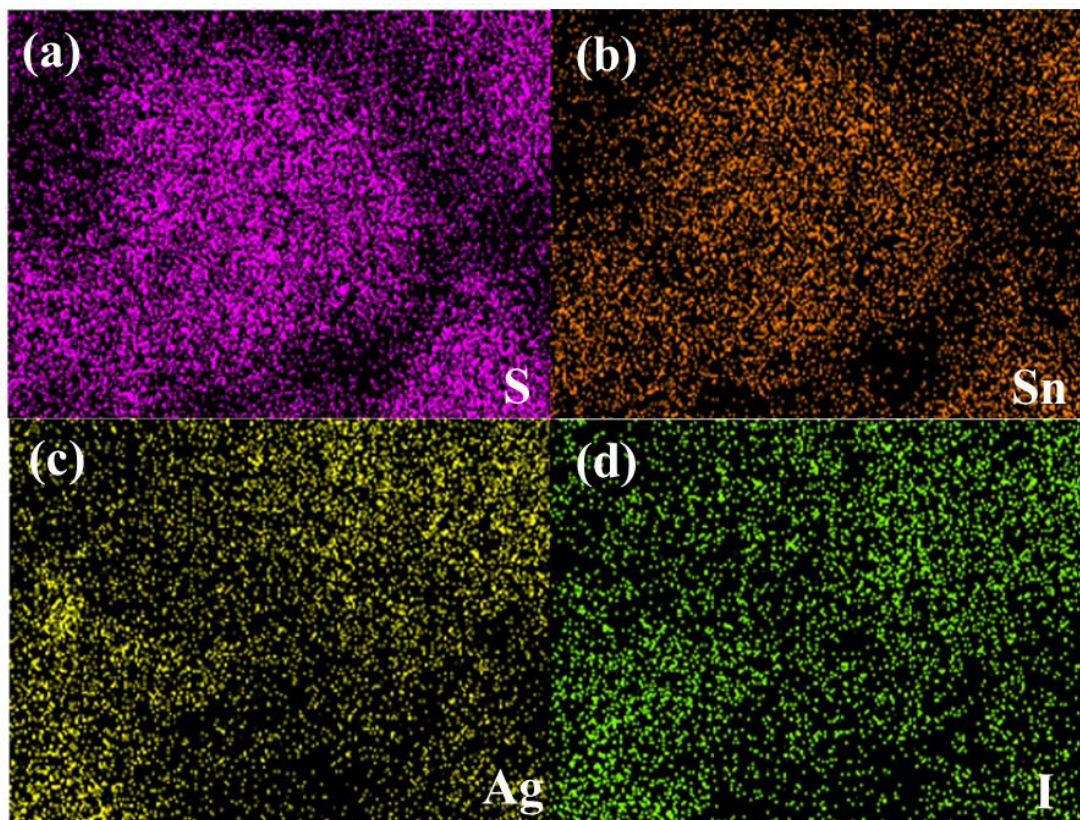


Figure 3. (a-d) The elemental mapping images of S, Sn, Ag and I of (80 wt%) AgI/SnS₂.

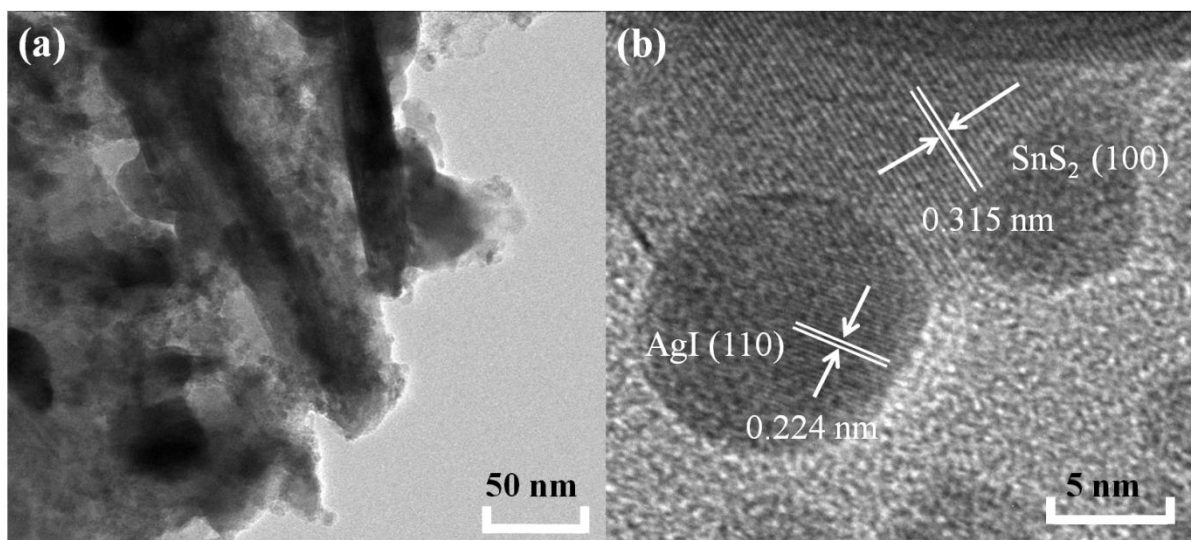


Figure 4. TEM (a) and HRTEM (b) images of (80 wt%) AgI/SnS₂ composites.

The detailed structures were also characterized by TEM and HRTEM. The TEM image in Fig. 4 (a) shows that amounts of AgI NPs covered on the surface of SnS₂ nanosheets. Moreover, two sets of different lattice spacing were observed in HRTEM image of AgI/SnS₂ (Fig. 4b). One set with

interplanar spacing of 0.315 nm was belonged to (100) plane of SnS₂, and the other one with interplanar spacing of 0.224 nm was corresponded to (110) plane of AgI. These results verified that the AgI/SnS₂ heterojunction was successfully established in composites, which was conducive to promoting the separation and transfer of photoinduced carriers.

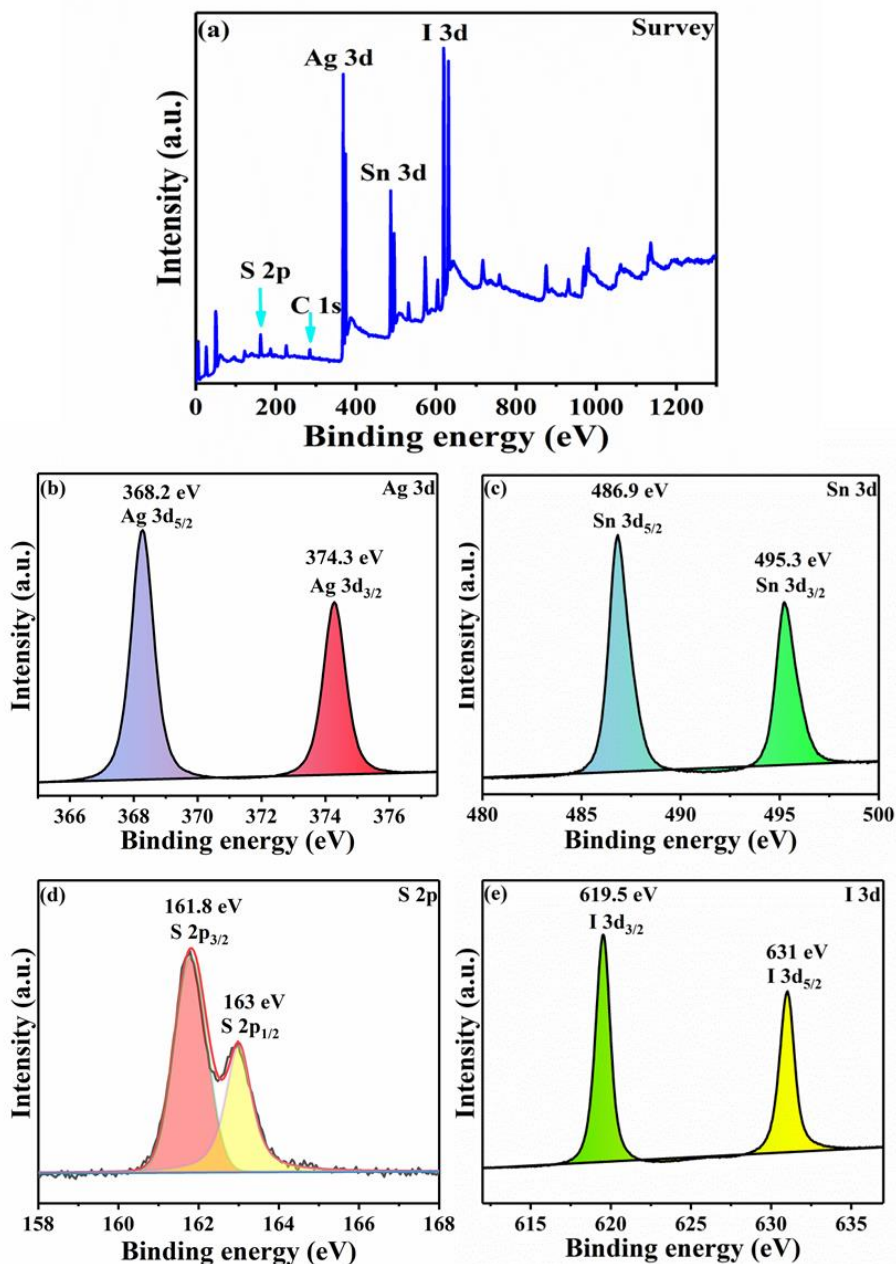


Figure 5. XPS spectra of (80 wt%) AgI/SnS₂ sample: (a) survey, (b) Ag 3d, (c) Sn 3d, (d) S 2p and (e) I 3d.

For analyzing the surface chemical composition and elemental valence state of AgI/SnS₂ composite, XPS studies were conducted. Fig. 5 (a) shows the survey spectra of composite, which revealed the coexistence of Ag, I, Sn, and S elements in the composites. In Fig. 5b, double peaks

observed at 368.2 and 374.3 eV can be indexed to Ag 3d_{5/2} and Ag 3d_{3/2}, respectively[36]. This result indicated that Ag exists in the form of Ag⁺. Fig. 5 (c) exhibits two peaks at the binding energy of 486.9 and 495.3 eV, belonged to Sn 3d_{5/2} and Sn 3d_{3/2}, respectively [37]. As for S (Fig. 5d), the binding energy peaks at 161.8 and 163.0 eV could be ascribed to S 2p_{3/2} and S 2p_{1/2} orbitals [26], respectively. Additionally, the signals of I 3d_{5/2} and I 3d_{3/2} (Fig. 5e) located at the binding energies of 631.0 and 619.5 eV, respectively, which were consistent with the reported values for pure AgI [29].

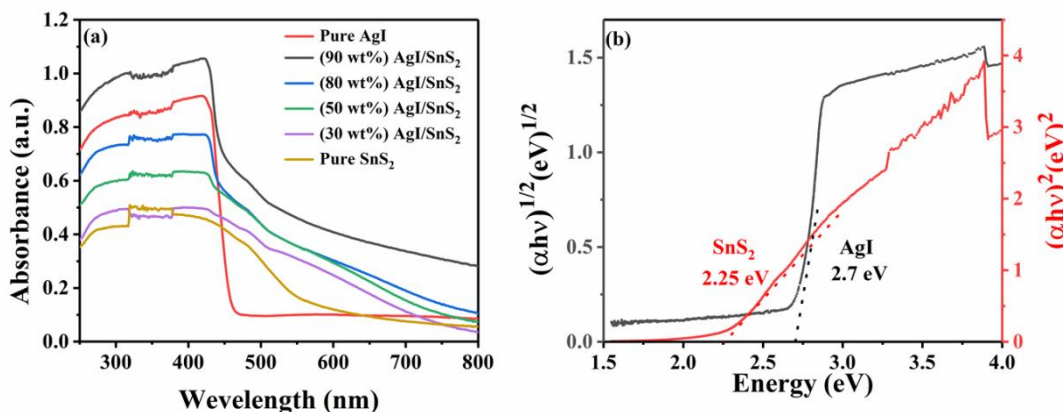


Figure 6. (a) UV-vis diffuses reflectance spectra of AgI, SnS₂ and AgI/SnS₂ composites and (b) plots of the $(\alpha h\nu)^{1/2}$ versus. photon energy ($h\nu$) for AgI and plots of the $(\alpha h\nu)^2$ versus. photon energy ($h\nu$) for SnS₂.

UV/Vis spectrometer was adopted to explore the optical properties of catalysts. As shown in Figure 6 (a), the absorption edge of the pristine AgI located at about 470 nm, which was consistent with the previous reports [31]. Pure SnS₂ displayed a superior absorption performance in the visible light area, and its absorption edge appeared at about 550 nm, which was also in good agreement with the reported studies[19, 26]. The absorption band edge of SnS₂ was longer than that of AgI, indicating it has relatively smaller band gap (Fig. 6b). Notably, after the precipitation of AgI on the surface of SnS₂, the optical absorption intensity of the composites was enhanced and the response range of visible light showed a little expanded. The improvement of visible light response could be attributed to the formation of the AgI/SnS₂ heterojunction, and will contribute to the utilization of more photons and thus enhance photocatalysis.

To explore the photocatalytic property of as-obtained catalysts, RhB was selected as a target pollutant for the photodegradation studies under visible light irradiation. As displayed in Fig. 7, ~64% of RhB on pure SnS₂ was decomposed within 50 min, while pure AgI degraded nearly 82% of RhB under the same conditions. Compared to pristine SnS₂ and AgI, the degradation efficiency of RhB over AgI/SnS₂ composites was significantly improved, which could be due to the well-established heterostructures between AgI and SnS₂. It was obvious that the amount of AgI was of great importance in the photodegradation process. For (30 wt%) AgI/SnS₂ and (50 wt%) AgI/SnS₂ composites, 84.4% and 90.3% of RhB were degraded, respectively. When the amount of AgI reached to 80 wt% in the composites, the (80 wt%) AgI/SnS₂ exhibited the highest photocatalytic performance for ~95% of RhB was removed in 50 min. This may be due to heterostructures formed between AgI and SnS₂, which was

useful to enhance the visible light absorption and promote the separation efficiency of photoexcited carriers. However, as the amount of AgI reached to 90 wt%, the photocatalytic performances decreased as compared to (80 wt%) AgI/SnS₂ composite (Fig.7). This result may be attributed to the possibility that excess AgI would performed as recombination centers, which caused high recombination of photogenerated carriers.

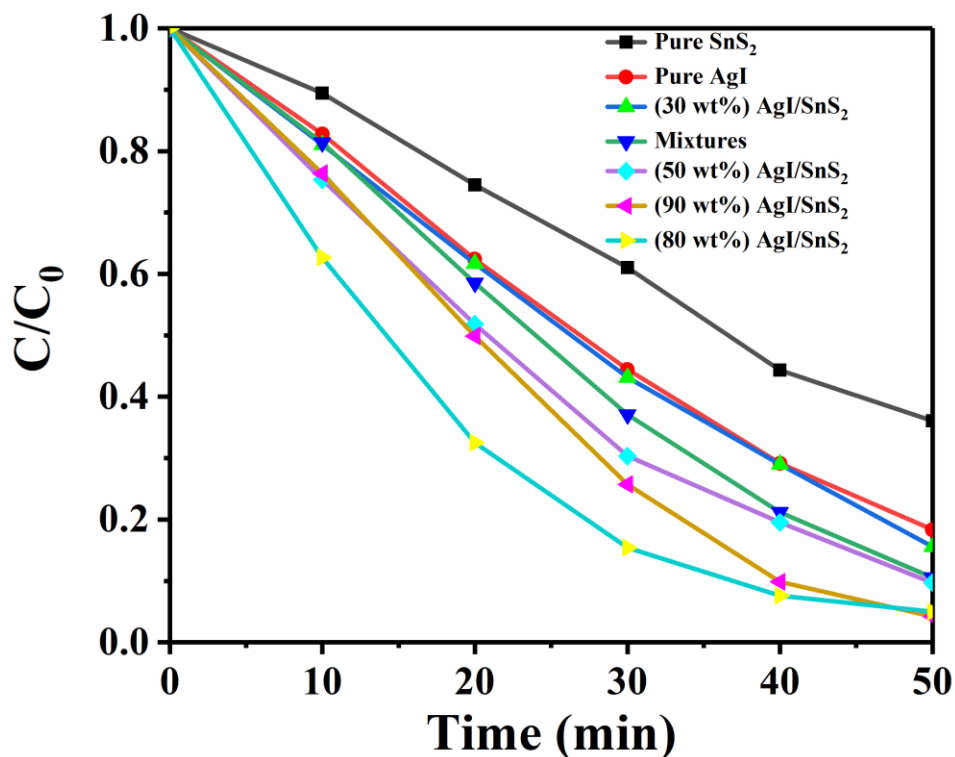


Figure 7. Photocatalytic degradation of RhB over different as-prepared samples under visible light irradiation.

The synergistic effect of AgI and SnS₂ in AgI/SnS₂ composites was also detected. In detail, 0.04 g AgI and 0.01 g SnS₂ were physically mixed and then used to decompose RhB under the same condition. As shown in Figure 7, 89.4% of RhB was degraded on the physically mixed sample within 50 min, which was lower than that of (80 wt%) AgI/SnS₂ heterojunctions. This result further proved that the heterojunctions formed between AgI and SnS₂ was vital to enhance the photocatalytic activity.

To detect the reaction kinetics of RhB degradation, the experimental data was analyzed by using the pseudo-first-order model: $\ln(C_0/C_t) = kt$ [38], where C_0 and C_t are the initial concentrations and residual concentrations at time t , respectively. The k denotes the kinetics constant. As shown in Fig. 8 (a), the slopes of all composites were higher than those of pure samples, suggesting the k values of composites were larger than those of pure samples. In addition, the k values of SnS₂, AgI, (90 wt%) AgI/SnS₂, (80 wt%) AgI/SnS₂, (50 wt%) AgI/SnS₂ and (30 wt%) AgI/SnS₂ was calculated to be 0.019 min⁻¹, 0.030 min⁻¹, 0.054 min⁻¹, 0.064 min⁻¹, 0.046 min⁻¹ and 0.036 min⁻¹, respectively (Fig. 8b). Remarkably, the k value of (80 wt%) AgI/SnS₂ was approximately 3.4 and 2.1 times as much as pure SnS₂ and AgI, respectively. These results indicated that loading AgI NPs onto the SnS₂ nanosheets can greatly elevate the photocatalytic efficiency of SnS₂.

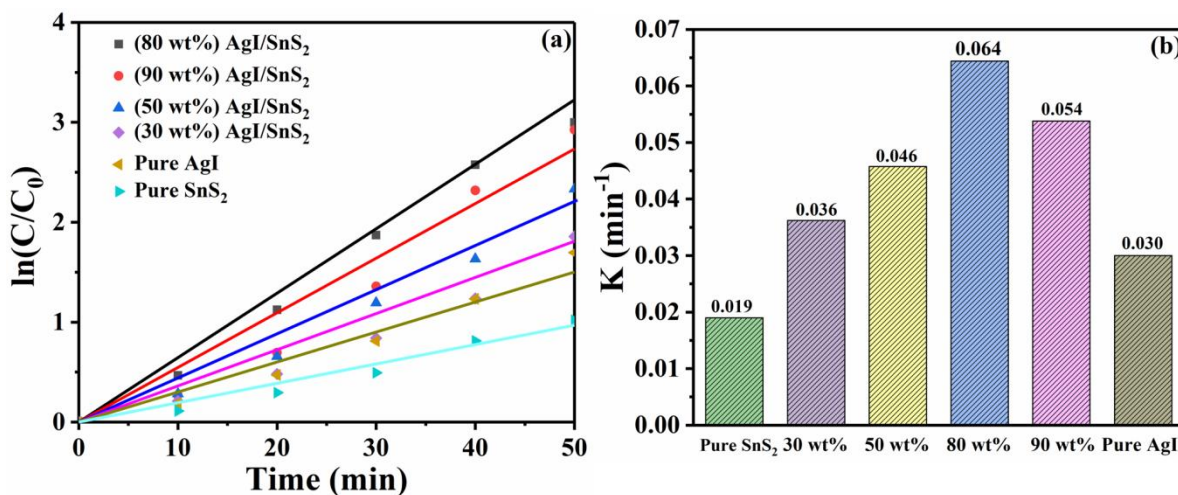


Figure 8. (a) Pseudo-first-order kinetics curves of RhB degradation over all samples and (b) values of reaction rate constant k .

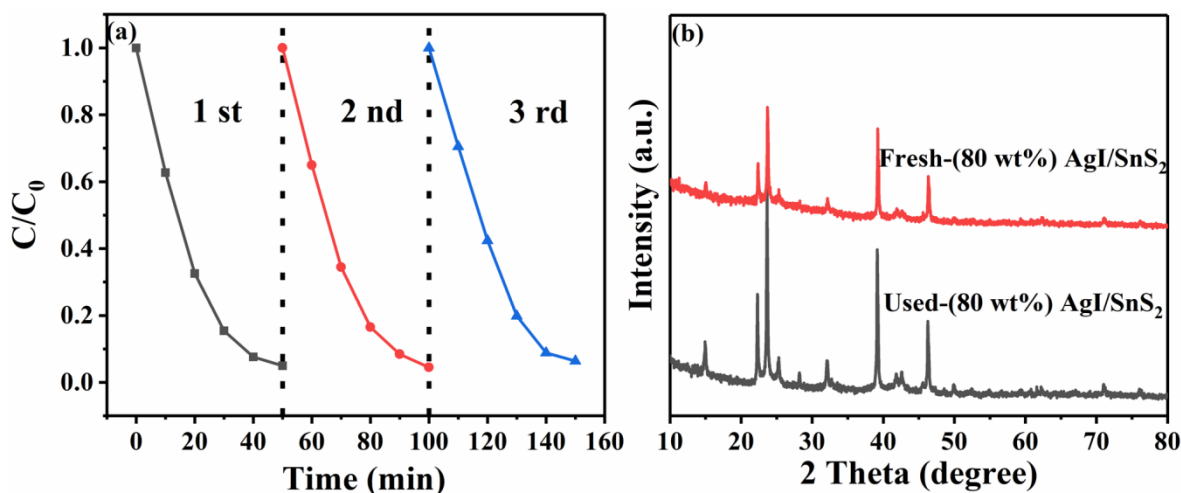


Figure 9. (a) Recycling tests on (80 wt%) AgI/SnS₂ composite under visible light irradiation and (b) XRD patterns of (80 wt%) AgI/SnS₂ sample before and after visible light irradiation.

For the purpose of evaluating the stability and reusability of the samples, the cycling experiment was executed. As displayed in Fig. 9 (a), after three cycling runs, the (80 wt%) AgI/SnS₂ composite remained high photocatalytic activity since the removal efficiency of RhB was 92.6%. Additionally, the chemical stability of (80 wt%) AgI/SnS₂ composite was also examined by XRD. From Fig. 9 (b), the phase structure of the used composite showed high similarity compared with that of fresh one after cycle experiment, indicating that (80 wt%) AgI/SnS₂ composite was a potential photostability material.

In the photodegradation reaction, electrons, holes (h^+), hydroxyl radical ($\bullet OH$) and superoxide radical ($\bullet O_2^-$) were four possible reaction species. To explore the potential mechanism of enhanced photocatalytic performance, it was necessary to ensure which one was the dominant active species in the photodegradation process. In experiments of active species trapping, isopropanol (IPA), triethanolamine (TEOA) and benzoquinone (BQ) were introduced as the scavengers of $\bullet OH$, h^+ and $\bullet O_2^-$ [39-41], respectively. As shown in Fig. 10, when IPA was introduced in the RhB solution, the

degradation efficiency of RhB only decreased by ~1.44% compared to the blank solution, indicating that $\bullet\text{OH}$ was not the activity specie in the degradation of RhB. Nevertheless, after the addition of TEOA and BQ, 74.67% and 27.45% of dyes were degraded, respectively, suggesting that h^+ and $\bullet\text{O}_2^-$ played significant roles in the photodegradation process.

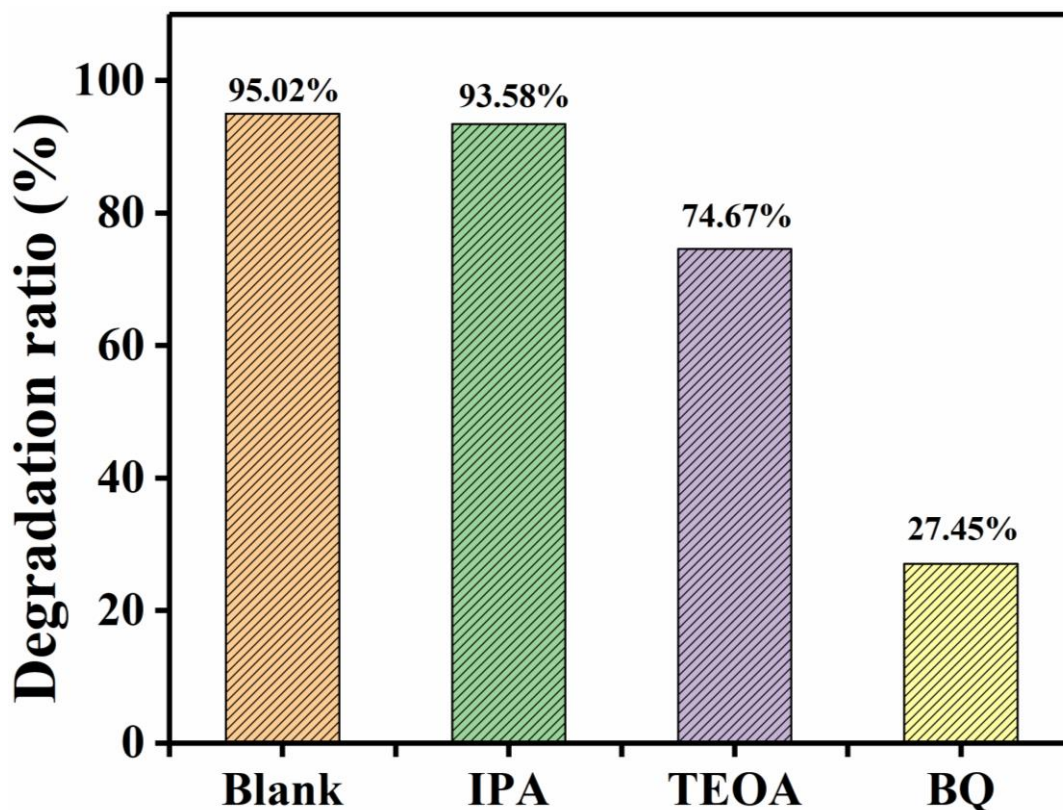


Figure 10. Effects of different scavengers on RhB degradation over (80 wt%) AgI/SnS₂ composite under visible light irradiation.

Photoluminescence (PL) spectra was utilized to understand the recombination of photoexcited carriers. It is well-established that the higher PL intensity indicates higher recomnination efficiency of photogenerated carriers[42]. Fig 11. shows the PL spectra of pure catalyst as well as (80 wt%) AgI/SnS₂ composite with the excitation wavelength of 320 nm. It was clearly that in comparison with pure SnS₂ and AgI, (80 wt%) AgI/SnS₂ composite exhibited much lower PL intensity, suggesting the separation efficiency of photoinduced carriers in composite was greatly improved. This may be attributed to the formed heterojunction between the two semiconductors, which can effectively retard the recombination of photoexcited carriers.

The band edge positions of SnS₂ and AgI were computed by the following formula:

$$E_{\text{VB}} = X - E_0 + 1/2E_{\text{g}} \quad (1)$$

$$E_{\text{CB}} = E_{\text{VB}} - E_{\text{g}} \quad (2)$$

where E_{VB} and E_{CB} refer to the VB and CB edge potential, X denotes the electronegativity of the materials (X values for SnS₂ and AgI are 4.66 eV [33] and 5.49 eV [27], respectively. E_0 signifies a constant (4.5 eV), and the E_{g} of SnS₂ and AgI were 2.25 and 2.70 eV. Based on the formulas, the $E_{\text{VB}}/$

E_{CB} of SnS_2 and AgI were calculated to be $-0.96/1.29$ eV and $-0.37/2.33$ eV, respectively. These results were nearly in accordance with the values reported previously [43, 44].

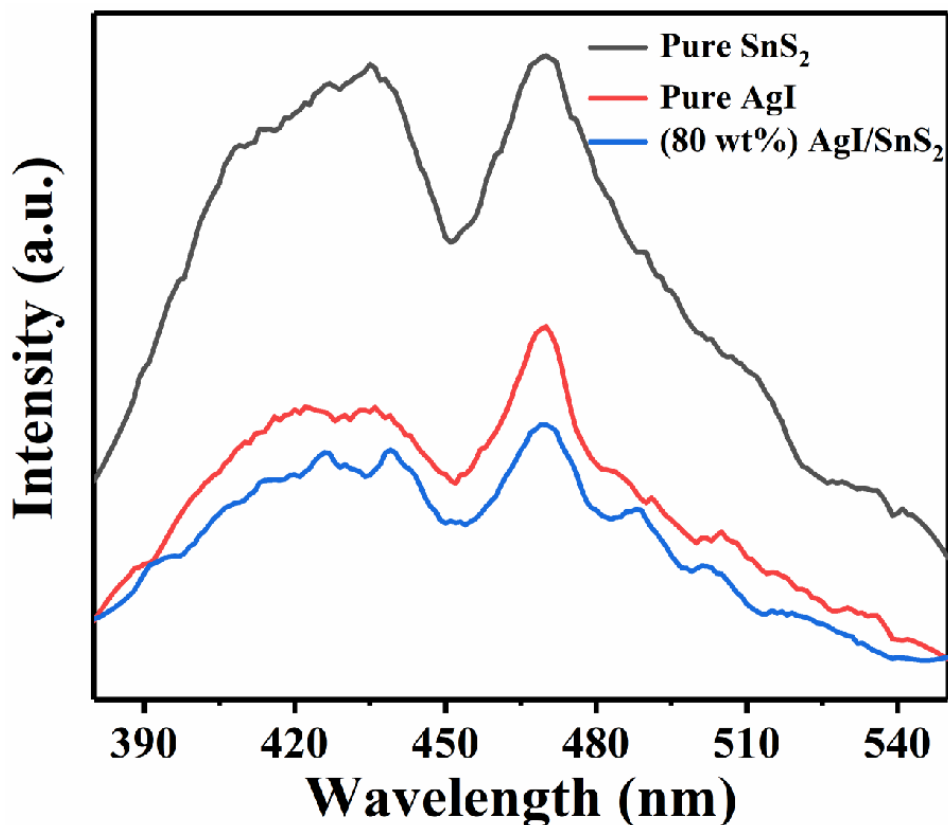


Figure 11. PL spectra of pure SnS_2 , pure AgI and (80 wt%) AgI/SnS_2 composite.

Based on the trapping experiments of active species and band structure analyses above, the band alignment of AgI/SnS_2 and possible mechanism were drawn out in the Fig. 12. When the AgI/SnS_2 composites were irradiated by visible light, both SnS_2 and AgI can generate e^- and h^+ . For the AgI/SnS_2 , both CB and VB potentials of SnS_2 were more negative than those of AgI . Therefore, the photogenerated electrons transferred to the CB of AgI from the CB of SnS_2 , and the h^+ in the VB of AgI migrated to the SnS_2 at the same time. As a result, the electron-hole pair separation efficiency was greatly improved. The e^- in the CB of AgI can react with the adsorbed O_2 to generate $\bullet\text{O}_2^-$ radicals since the CB potential of AgI (-0.41 eV) was more negative than the potential of $\text{O}_2/\bullet\text{O}_2^-$ (-0.046 eV)[45]. However, as the VB potential of SnS_2 (1.26 eV) was more negative than that of $\text{H}_2\text{O}/\bullet\text{OH}$ (2.37 eV)[46], the $\bullet\text{OH}$ generation was prohibited. Hence, $\bullet\text{O}_2^-$ and h^+ were the dominant active oxidative species, which were crucial for the RhB decomposition. This result was consistent with the outcomes of the radical trapping.

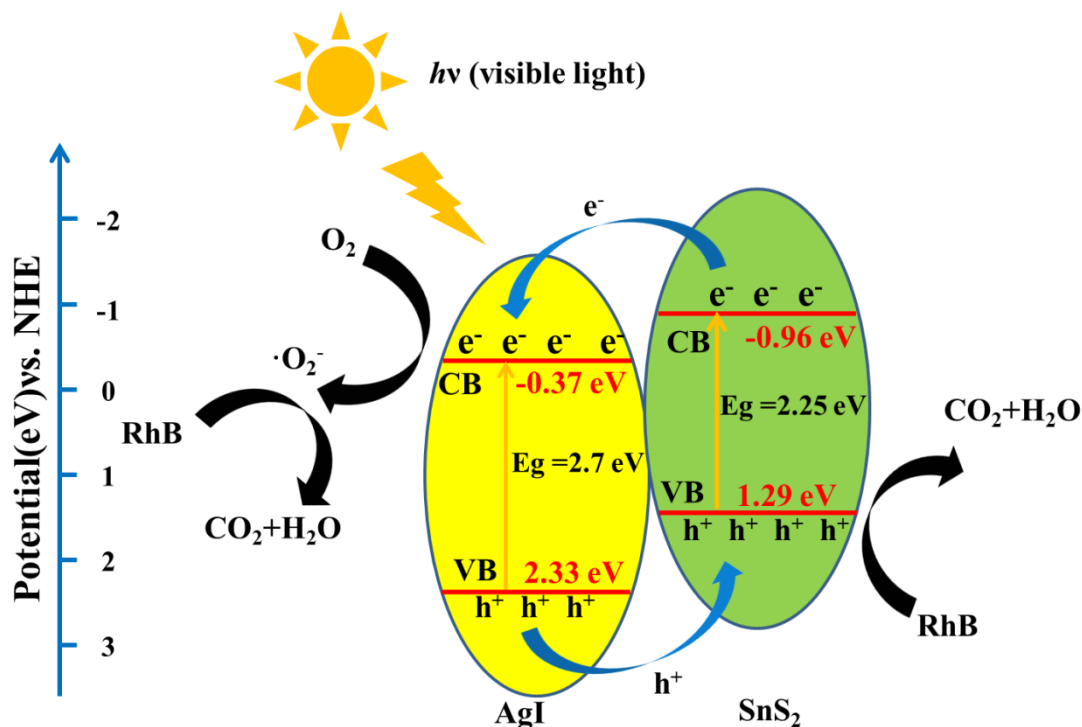


Figure 12. Schematic diagrams of energy band of SnS₂ and AgI and the possible carriers separation process under visible light irradiation.

4. CONCLUSION

To summarize, novel and stable AgI/SnS₂ hybrid materials with different mass percentage of AgI were successfully prepared through a facile solvothermal-precipitation strategy. The AgI/SnS₂ composites exhibited outstanding photocatalytic performances for removal of RhB with illumination of visible light. Notably, (80% wt%) AgI/SnS₂ displayed the highest rate constant of 0.064 min⁻¹, which was about 2.1 and 3.4 times higher than pure AgI NPs and SnS₂ nanosheets, respectively. The improvement of photocatalytic efficiency could result from the higher charge carriers' separation efficiency, which was attributed to the synergistic effect between AgI and SnS₂. Besides, the $\cdot\text{O}_2^-$ and h^+ were recognized as the main reactive species in the process of photodegradation, and a possible photocatalytic mechanism was proposed based on the experimental results. The (80% wt%) AgI/SnS₂ sample also displayed good stability. This investigation demonstrates that the AgI/SnS₂ heterojunctions possess potential applications in organic pollutant removal.

ACKNOWLEDGEMENTS

We gratefully acknowledge the financial support of the Natural Science Foundation of Anhui Province (1908085QF293 and 1908085QA36) and Foundation of Educational Commission of Anhui Province (KJ2018A0394, KJ2018A0393, KJ2016SD53 and KJ2019B14).

References

1. M.J. Hao, T.T. Yi, Y.F. Cao, Y.M. Song, Z.Z. Cao, W.Y. He, Y.F. Gao and J.R. Liu, *Adv. Powder Technol.*, 30 (2019) 111.

2. B.B. Shao, X.J. Liu, Z.F. Liu, G.M. Zeng, Q.H. Liang, C. Liang, Y. Cheng, W. Zhang, Y. Liu and S.X. Gong, *Chem. Eng. J.*, 368 (2019) 730.
3. Y. Jin, D. L. Jiang, D. Li, P. Xiao, X.D. Ma and M. Chen, *ACS Sustainable Chem. Eng.*, 5 (2017) 9749.
4. M. Yan, Y.L. Wu, Y. Yan, X. Yan, F.F. Zhu, Y.Q. Hua and W.D. Shi, *ACS Sustainable Chem. Eng.*, 4 (2015) 757.
5. X. Zhang, J. Zhang, J.Q. Yu, Y. Zhang, Z.X. Cui, Y. Sun and B.R. Hou, *Appl. Catal., B*, 220 (2018) 57.
6. H. Ma, Q.Y. Liu, B. Zhang, R.J. Zhang, Z.Y. Chen, Y.Q. Li, W.Q. Shao, X.Y. Wu, Y.C. Zhang and W.N. Ye, *J. Nanosci. Nanotechnol.*, 19 (2019) 7859.
7. W.D. Zhang, X.A. Dong, B. Jia, J.B. Zhong, Y.J. Sun and F. Dong, *Appl. Surf. Sci.*, 430 (2018) 571.
8. Y. Zhao, X. Huang, X. Tan, T. Yu, X.L. Li, L.B. Yang and S.C. Wang, *Appl. Surf. Sci.*, 365 (2016) 209.
9. W. Teng, X.J. Tan, X.Y. Li and Y.B. Tang, *Appl. Surf. Sci.*, 409 (2017) 250.
10. M.E. Taheri, A. Petala, Z. Frontistis, D. Mantzavinos and D. Kondarides, *Catal. Today*, 280 (2017) 99.
11. S.S. Ma, J.J. Xue, Y.M. Zhou and Z.W. Zhang, *J. Mater. Chem. A*, 2 (2014) 7272.
12. L. Tang, C.Y. Feng, Y.C. Deng, G.M. Zeng, J.J. Wang, Y.N. Liu, H.P. Feng and J.J. Wang, *Appl. Catal., B*, 230 (2018) 102.
13. B. Barrocas, T.J. Entradas, C.D. Nunes and O.C. Monteiro, *Appl. Catal., B*, 218 (2017) 709.
14. J. Rong, T. Zhang, F.X. Qiu, X.S. Rong, X.L. Zhu and X.Y. Zhang, *J. Alloys Compd.*, 685 (2016) 812.
15. Y. Feng, X. Yan, C.B. Liu, Y.Z. Hong, L. Zhu, M.J. Zhou and W.D. Shi, *Appl. Surf. Sci.*, 353 (2015) 87.
16. S. Park, J.H. Park, R. Selvaraj and Y. Kim, *J. Ind. Eng. Chem.*, 31 (2015) 269.
17. F.Z. Qiu, W.J. Li, F.Z. Wang, H.D. Li, X.T. Liu and J.Y. Sun, *J. Colloid Interface Sci.*, 493 (2017) 1.
18. T.M. Di, B.C. Zhu, B. Cheng, J.G. Yu and J.S. Xu, *J. Catal.*, 352 (2017) 532.
19. H. Meng, T.T. Wang, H.B. Chen, Y.Z. Liu, X. Yu, Y. Zhu and Y.M. Zhang, *Nano*, 11 (2016) 1650087.
20. J. Yu, C.Y. Xu, F.X. Ma, S.P. Hu, Y.W. Zhang and L. Zhen, *ACS Appl. Mater. Interfaces*, 6 (2014) 22370.
21. L. Jing, Y. Xu, M. Zhang, M. Xie, H. Xu, M. Hu, J. Liu, S. Huang and H. Li, *Inorg. Chem. Front.*, 5 (2018) 63.
22. G.B. Liu, Y.F. Qiu, Z.G. Wang, J. Zhang, X.S. Chen, M.J. Dai, D.C. Jia, Y. Zhou, Z.H. Li and P.A. Hu, *ACS Appl. Mater. Interfaces*, 9 (2017) 37750.
23. X.D. Cui, W.W. Xu, Z.Q. Xie, J.A. Dorman, M.T.G. Wing and Y. Wang, *Dalton Trans.*, 45 (2016) 16290.
24. Y. Zhang and S. Park, *J. Mater. Chem. A*, 6 (2018) 20304.
25. Y. Yang, X.A. Yang, D. Leng, S.B. Wang and W.B. Zhang, *Chem. Eng. J.*, 335 (2018) 491.
26. J. Luo, X.S. Zhou, L. Ma, X.Y. Xu, J.X. Wu and H.P. Liang, *Mater. Res. Bull.*, 77 (2016) 291.
27. W.J. Xue, Z.W. Peng, D.L. Huang, G.M. Zeng, X.J. Wen, R. Deng, Y. Yang and X.L. Yan, *Ceram. Int.*, 45 (2019) 6340.
28. J.L. Liang, F.Y. Liu, J. Deng, M. Li and M.P. Tong, *Water Res.*, 123 (2017) 632.
29. Q. Wang, X.D. Shi, J.J. Xu, J.C. Crittenden, E.Q. Liu, Y. Zhang and Y.Q. Cong, *J. Hazard. Mater.*, 307 (2016) 213.
30. L. Liu, Y.H. Qi, J.Y. Yang, W.Q. Cui, X.G. Li and Z.S. Zhang, *Appl. Surf. Sci.*, 358 (2015) 319.
31. Z. Zhang, D. Jiang, C. Xing, L. Chen, M. Chen and M.Q. He, *Dalton Trans.*, 44 (2015) 11582.
32. X.J. Wen, C.G. Niu, M. Ruan, L. Zhang and G.M. Zeng, *J. Colloid Interface Sci.*, 497 (2017) 368.
33. H.J. Liu, C.W. Du, H.K. Bai, Y.Z. Su, D.D. Wei, Y.Q. Wang, G.G. Liu and L. Yang, *J. Mater. Sci.*, 53 (2018) 10743.

34. L.X. Hu, F.Y. Chen, P.F. Hu, L.P. Zou and X. Hu, *J. Mol. Catal. A: Chem.*, 411 (2016) 203.
35. Z. Wan and G. Zhang, *J. Mater. Chem. A*, 3 (2015) 16737.
36. C. Liang, C. Niu, H. Guo, D. Huang, X. Wen, S. Yang and G. Zeng, *Catal. Sci. Technol.*, 8 (2018) 1161.
37. J. Zhang, L.L. Zhang, Y.X. Shi, G.L. Xu, E.P. Zhang, H.B. Wang, Z. Kong, J.H. Xi and Z.G. Ji, *Appl. Surf. Sci.*, 420 (2017) 839.
38. X.Z. Yuan, Z.B. Wu, G.M. Zeng, L.B. Jiang, J. Zhang, T. Xiong, H. Wang and D. Mo, *Appl. Surf. Sci.*, 454 (2018) 293.
39. X.J. Yuan, D.Y. Shen, Q. Zhang, H.B. Zou, Z.L. Liu and F. Peng, *Chem. Eng. J.*, 369 (2019) 292.
40. K. Li, Y.J. Liang, J. Yang, H. Zhang, G. Yang and W. Lei, *J. Photochem. Photobiol., A*, 364 (2018) 240.
41. J.L. Lv, K. Dai, J.F. Zhang, Q. Liu, C.H. Liang and G.P. Zhu, *Sep. Purif. Technol.*, 178 (2017) 6.
42. M. Yan, Y.Q. Hua, F.F. Zhu, W. Gu, J.H. Jiang, H.Q. Shen and W.D. Shi, *Appl. Catal., B*, 202 (2017) 518.
43. X.H. Wang, J. Yang, S.Q. Ma, D. Zhao, J. Dai and D.F. Zhang, *Catal. Sci. Technol.*, 6 (2016) 243.
44. J. Luo, X.S. Zhou, L. Ma, L.M. Xu, X.Y. Xu, Z.H. Du and J.Q. Zhang, *Mater. Res. Bull.*, 81 (2016) 16.
45. X.Y. Gao, G.B. Tang, W. Peng, Q. Guo and Y.M. Luo, *Chem. Eng. J.*, 360 (2019) 1320.
46. Z. Xiang, J.B. Zhong, S.T. Huang, J.Z. Li, J.F. Chen, T. Wang, M.J. Li and P. Wang, *Mater. Sci. Semicond. Process.*, 52 (2016) 62

© 2020 The Authors. Published by ESG (www.electrochemsci.org). This article is an open access article distributed under the terms and conditions of the Creative Commons Attribution license (<http://creativecommons.org/licenses/by/4.0/>).